Computers and Fluids 131 (2016) 45–55

Contents lists available at ScienceDirect

Computers and Fluids

journal homepage: www.elsevier.com/locate/compfluid

A compressible lattice Boltzmann finite volume model for high subsonic and transonic flows on regular lattices

Yongliang Feng[a,b], Pierre Sagaut[c], Wen-Quan Tao[a,*]

[a] Key Laboratory of Thermo-fluid Science and Engineering of MOE School of Energy & Power Engineering, Xi'an Jiaotong University, Xi'an 710049, China
[b] Institut Jean le Rond d'Alembert, UMR 7190, Université Pierre et Marie Curie, 4 place Jussieu-case 162, F-75252, France
[c] Aix-Marseille Université, CNRS, Centrale Marseille, M2P2 UMR 7340, 13451 Marseille, France

ARTICLE INFO

Article history:
Received 15 July 2015
Revised 19 January 2016
Accepted 10 March 2016
Available online 15 March 2016

Keywords:
Lattice Boltzmann
Compressible
Shock wave
Double distribution function

ABSTRACT

A multi-dimensional double distribution function thermal lattice Boltzmann model has been developed to simulate fully compressible flows at moderate Mach number. The lattice Boltzmann equation is temporally and spatially discretizated by an asymptotic preserving finite volume scheme. The micro-velocities discretization is adopted on regular low-symmetry lattices (D1Q3, D2Q9, D3Q15, D3Q19, D3Q27). The third-order Hermite polynomial density distribution function on low-symmetry lattices is used to solve the flow field, while a second-order energy distribution is employed to compute the temperature field. The fully compressible Navier–Stokes equations are recovered by standard order Gauss–Hermite polynomial expansions of Maxwell distribution with cubic correction terms, which are added by an external force expressed in orthogonal polynomials form. The proposed model is validated considering several benchmark cases, namely the Sod shock tube, thermal Couette flow and two-dimensional Riemann problem. The numerical results are in very good agreement with both analytical solution and reference results.

1. Introduction

The lattice Boltzmann method (LBM) is a recently developed method for simulation fluid flows and complicated physical phenomena. During the past two decades, the lattice Boltzmann (LB) method has attracted exponentially growing attention and interest. There has been rapid progress in developing new models and applications in many fields, e.g., [1–5]. The LB method has achieved great success in simulating nearly incompressible and isothermal fluid flows. There has also been an ongoing effort in the construction of stable thermal compressible lattice Boltzmann equation models in order to simulate heat transfer and compressible flows. However, it appears to be very difficult to model realistic thermal compressible flows with enough satisfaction in continuum and slip flow regimes [6–9].

The setup of discrete velocities and the determination of equilibrium distribution functions are two key issues for the construction of the LB models. The equilibrium distribution function is usually a truncated polynomial expression, which can be derived by applying the truncated Taylor series expansion in terms of the Mach number or a projection onto a finite polynomial basis to the exponential form of the Maxwellian function. The second-order polynomial in terms of particle speed and flow velocity is used in the common isothermal models [1]. Higher order velocity terms must be included for compressible models [2,10]. A theoretical framework was presented for representing hydrodynamic systems through a systematic discretization of the Boltzmann kinetic equation by means of Hermite tensor expansion of the Maxwellian function in [11].

High subsonic and transonic flows are very common in aerodynamics or aerospace engineering. The low-symmetry lattices (D1Q3, D2Q9, D3Q15, D3Q19, D3Q27) are restricted to a free-stream Mach number value of about 0.4. Many multi-speed higher order thermal lattice models have been proposed for transonic, supersonic and hypersonic flows, such as D2Q25, D2Q37, D3Q39 and D3Q125 [12]. Efforts to reduce discrete velocities of thermal lattice models considering compressible flows with evolving temperatures at larger Mach numbers met with limited success for improving computing efficiency. A linear stability analysis for the multi-speed lattice Boltzmann models has been presented in [13,14]. A multi-speed lattice Boltzmann/finite-difference hybrid method has been developed for transonic flows in [15]. An extended lattice Boltzmann methodology for high subsonic jet has been studied in [16]. A dual entropy approach stable lattice Boltzmann scheme for mono-dimensional nonlinear waves has been presented in [17]. A compressible thermal lattice

* Corresponding author. Tel.: +86 29 8266 9106; fax: +86 29 8266 9106.
E-mail addresses: pierre.sagaut@univ-amu.fr (P. Sagaut), wqtao@mail.xjtu.edu.cn (W.-Q. Tao).

http://dx.doi.org/10.1016/j.compfluid.2016.03.009
0045-7930/

Boltzmann model with factorization symmetry for supersonic flow has been proposed in [19]. Recently a multi-speed entropic lattice Boltzmann model has been presented for moderate Mach number thermal flows [20].

Compared with the conventional computational fluid dynamics methods which are based on Navier–Stokes equations, LBM has many distinctive features, such as simple algorithm, efficient unsteady flow solver with high accuracy, parallel in nature and simple fluid–solid/fluid interaction [3–5]. As authors' knowledge, part of those advantages will be less important when the micro-velocities increases. Usually, those low symmetry lattices model (D1Q3, D2Q9, D3Q15, D3Q19, D3Q27) are regarded as "regular" or "'standard" lattice model, in which the magnitude of micro-velocities are generally less than grid size and nearest neighbor nodes are required in propagation-streaming procedure [18,21,22].

Several extended lattice Boltzmann models based on regular lattice were proposed for simulation of low Mach number flows with significant density changes [21–23]. Feng et al. [18] extended the coupled DDF-BGK model to three-dimensional case with a general correction term without cubic defects. However, it should be pointed out that most of the previous thermal compressible LB models on regular lattice were proposed for weakly compressible flows only.

Despite the fact that many efforts have been made from various viewpoints, an efficient and of satisfactory lattice Boltzmann method for thermal compressible flows in high subsonic and transonic regimes is still missing. The purpose of this paper is to develop a multi-dimensional LB method for the simulation of fully compressible fluid flows in high subsonic and transonic limit on regular D1Q3, D2Q9, D3Q15,D3Q19, and D3Q27 lattices.

This paper is organized as follows. The new original DDF Boltzmann-BGK model is presented in Section 2. Numerical results obtained for benchmark cases are displayed in Section 3. Finally, some conclusions are given in Section 4.

2. The double distribution function Boltzmann-BGK model

The double distribution function (DDF) themal lattice Boltmann models were proposed for reducing discrete velocities and adjust Prandtl number, which are the main disadvantages of multi-speed thermal models. In this section, we briefly describe the coupled kinetic model equations based on DDFs for the later development of thermal LBM. The two relaxation times kinetic model equations were proposed and discussed in [7,8,24]. The DDF Boltzmann-BGK equation in terms of two relaxation times can be expressed as follows:

$$\frac{\partial f}{\partial t}+\boldsymbol{\xi}\cdot\frac{\partial f}{\partial \boldsymbol{x}}=-\frac{1}{\tau_f}(f-f^{eq}) \tag{1}$$

$$\frac{\partial h}{\partial t}+\boldsymbol{\xi}\cdot\frac{\partial h}{\partial \boldsymbol{x}}=-\frac{1}{\tau_h}(h-h^{eq})-\frac{1}{\tau_{hf}}(h') \tag{2}$$

where $h'=\boldsymbol{\xi}\cdot\boldsymbol{u}-\frac{1}{2}u^2(f-f^{eq})$ in Guo's model [8] and $h'=\frac{w_i}{RT_0}\boldsymbol{\xi}\cdot\boldsymbol{u}(\boldsymbol{P}-\boldsymbol{P}^{eq})$ in Karlin's consistent model [24], where $\boldsymbol{P}^{eq}$, $\boldsymbol{P}$ represents equilibrium part of stress tensor and stress tensor, respectively. Guo's model and Karlin's model lead to the same Navier–Stokes–Fourier equations in the hydrodynamic limit. Guo's model is adopted in this paper. The equilibrium density distribution function f^{eq} and equilibrium total energy distribution function h^{eq} are given by

$$f^{eq}=\rho\left(\frac{1}{2\pi RT}\right)^{\frac{D}{2}}\exp\left(\frac{(\boldsymbol{\xi}-\boldsymbol{u})^2}{2RT}\right) \tag{3}$$

$$h^{eq}=\frac{\rho\xi^2}{2}\left(\frac{1}{2\pi RT}\right)^{\frac{D}{2}}\exp\left(\frac{(\boldsymbol{\xi}-\boldsymbol{u})^2}{2RT}\right) \tag{4}$$

in which $\rho(\boldsymbol{x},t)$, $\boldsymbol{u}(\boldsymbol{x},t)$, $T(\boldsymbol{x},t)$ denote the usual macroscopic quantities, i.e., the density, fluid velocity and temperature of the gas, respectively. $\boldsymbol{\xi}$ is the particle velocity, R the gas constant and D is the space dimension. $f(\boldsymbol{\xi},\boldsymbol{x},t)$ is the usual density distribution function, and $h(\boldsymbol{\xi},\boldsymbol{x},t)=\boldsymbol{\xi}^2 f/2$ is the total energy distribution function. τ_f and τ_h stand for the momentum and total energy collision relaxation times. The relaxation times are tied by the following relation: $1/\tau_{hf}=1/\tau_h-1/\tau_f$.

Once the distribution functions f and h are known, the macroscopic quantities, e.g., the density ρ, mean velocity u and temperature T are defined

$$\rho=\int f d\boldsymbol{\xi} \tag{5}$$

$$\rho\boldsymbol{u}=\int \boldsymbol{\xi} f d\boldsymbol{\xi} \tag{6}$$

$$\frac{D}{2}\rho RT=\int h d\boldsymbol{\xi}-\frac{\rho u^2}{2} \tag{7}$$

Through the Chapman–Enskog expansion of the distribution function, one can recover the thermal compressible Navier–Stokes equations and energy conservation equation at the second order of approximation:

$$\frac{\partial \rho}{\partial t}+\nabla\cdot(\rho\boldsymbol{u})=0 \tag{8}$$

$$\frac{\partial \rho\boldsymbol{u}}{\partial t}+\nabla\cdot(\rho\boldsymbol{u}\boldsymbol{u})=-\nabla p+\nabla\cdot\Pi \tag{9}$$

$$\frac{\partial \rho E}{\partial t}+\nabla\cdot((\rho E+p)\boldsymbol{u})=\nabla\cdot(\lambda\nabla T)+\nabla\cdot(\boldsymbol{u}\cdot\Pi) \tag{10}$$

where the viscous stress tensor Π is given by

$$\Pi=\mu\left[\nabla\boldsymbol{u}+(\nabla\boldsymbol{u})^T-\frac{2}{D}(\nabla\cdot\boldsymbol{u})\boldsymbol{I}\right] \tag{11}$$

where $\boldsymbol{I}$ is unit tensor.

The perfect gas equation of state $p=\rho RT$ is also recovered, and the dynamic viscosity and thermal conductivity are defined as

$$\mu=\tau_f p \tag{12}$$

$$\lambda=\frac{(D+2)R}{2}\tau_h p \tag{13}$$

showing the consistency of the DDF model.

2.1. Lattice discrete velocity model

Following the approach proposed in [11], the Grad's moment expansion approach is adopted by expanding $f(\boldsymbol{x},\boldsymbol{\xi},t)$ and $h(\boldsymbol{x},\boldsymbol{\xi},t)$ in terms of Hermite polynomials,

$$f=\omega(\xi,T)\sum_{n=0}^{\infty}\frac{1}{n!}\boldsymbol{a}^{(n)}\mathcal{H}^{(n)}(\boldsymbol{\xi}) \tag{14}$$

$$h=\omega(\xi,T)\sum_{n=0}^{\infty}\frac{1}{n!}\boldsymbol{b}^{(n)}\mathcal{H}^{(n)}(\boldsymbol{\xi}) \tag{15}$$

where

$$\omega(\boldsymbol{\xi},T)=\frac{1}{(2\pi)^{D/2}}e^{-\boldsymbol{\xi}^2/2} \tag{16}$$

is the weighting function, $\boldsymbol{a}^{(n)}$, $\boldsymbol{b}^{(n)}$ and $\mathcal{H}^{(n)}(\boldsymbol{\xi})$ are rank-n tensors. The expansion coefficients $\boldsymbol{a}^{(n)}$ and $\boldsymbol{b}^{(n)}$ are given by the following projections:

$$\boldsymbol{a}^{(n)}=\int f\mathcal{H}^{(n)}(\boldsymbol{\xi})d\boldsymbol{\xi} \tag{17}$$

$$\boldsymbol{b}^{(n)} = \int h\mathcal{H}^{(n)}(\boldsymbol{\xi})d\boldsymbol{\xi} \tag{18}$$

Similarly, the equilibrium distribution functions $f^{(0)}(\boldsymbol{x}, \boldsymbol{\xi}, t)$ and $h^{(0)}(\boldsymbol{x}, \boldsymbol{\xi}, t)$ are also expanded to the same orders as follows:

$$f^{(0)} = \omega(\boldsymbol{\xi}, T)\sum_{n=0}^{\infty}\frac{1}{n!}\boldsymbol{a}_0^{(n)}\mathcal{H}^{(n)}(\boldsymbol{\xi}) \tag{19}$$

$$h^{(0)} = \omega(\boldsymbol{\xi}, T)\sum_{n=0}^{\infty}\frac{1}{n!}\boldsymbol{b}_0^{(n)}\mathcal{H}^{(n)}(\boldsymbol{\xi}) \tag{20}$$

The expansion coefficients $\boldsymbol{a_0}^{(n)}$ and $\boldsymbol{b_0}^{(n)}$ are given by

$$\boldsymbol{a}_0^{(n)} = \int f^{(0)}\mathcal{H}^{(n)}(\boldsymbol{\xi})d\boldsymbol{\xi} \tag{21}$$

$$\boldsymbol{b}_0^{(n)} = \int h^{(0)}\mathcal{H}^{(n)}(\boldsymbol{\xi})d\boldsymbol{\xi} \tag{22}$$

The Hermite expansion coefficients $\boldsymbol{a}_0^{(n)}$ and $\boldsymbol{b}_0^{(n)}$ can be explicitly calculated as

$$\begin{aligned}
\boldsymbol{a}_0^{(0)} &= \rho,\\
\boldsymbol{a}_0^{(1)} &= \rho\boldsymbol{u},\\
\boldsymbol{a}_0^{(2)} &= \rho[\boldsymbol{uu} + (RT-1)\delta],\\
\boldsymbol{a}_0^{(3)} &= \rho[\boldsymbol{uuu} + (RT-1)\delta\boldsymbol{u}].\\
\boldsymbol{b}_0^{(0)} &= \rho E,\\
\boldsymbol{b}_0^{(1)} &= (p+\rho E)\boldsymbol{u},\\
\boldsymbol{b}_0^{(2)} &= (2p+\rho E)\boldsymbol{uu} + [pRT + \rho E(RT-1)]\delta.
\end{aligned}$$

where δ denotes the Kronecker symbol with arbitrary dimension.

To obtain a tractable method, one must truncate these infinite expansions to desired orders. We refer the truncation order of the density and energy distribution functions as N_f and N_h, respectively. In this paper, it is proposed to take $N_f = 3$ for density distribution function and $N_h = 2$ for energy distribution function. After some algebra, one obtains the following expressions, in which $\theta = T/T_0$:

$$\begin{aligned}
f^{eq,3} = \omega(\boldsymbol{\xi}, T_0)\rho\Bigg\{1 &+ \frac{\boldsymbol{\xi}\cdot\boldsymbol{u}}{RT_0} + \frac{1}{2}\left(\frac{\boldsymbol{\xi}\cdot\boldsymbol{u}}{RT_0}\right)^2 - \frac{\boldsymbol{u}^2}{2RT_0}\\
&+ \frac{\theta-1}{2}\left(\frac{\boldsymbol{\xi}^2}{RT_0} - D\right) + \frac{\boldsymbol{\xi}\cdot\boldsymbol{u}}{6RT_0}\left[\left(\frac{\boldsymbol{\xi}\cdot\boldsymbol{u}}{RT_0}\right)^2\right.\\
&\left. - \frac{3\boldsymbol{u}^2}{RT_0} + 3(\theta-1)\left(\frac{\boldsymbol{\xi}^2}{RT_0} - D - 2\right)\right]\Bigg\}
\end{aligned} \tag{23}$$

$$\begin{aligned}
h^{eq,2} = Ef^{eq} + \omega(\boldsymbol{\xi}, T_0)p\Bigg[&\frac{\boldsymbol{\xi}\cdot\boldsymbol{u}}{RT_0} + \left(\frac{\boldsymbol{\xi}\cdot\boldsymbol{u}}{RT_0}\right)^2\\
&- \frac{\boldsymbol{u}^2}{RT_0} + \frac{\theta}{2}\left(\frac{\boldsymbol{\xi}^2}{RT_0} - D\right)\Bigg]
\end{aligned} \tag{24}$$

For regular low symmetry lattices, the lattice tensor $\boldsymbol{E}^{(n)} = \sum_{\alpha}(\boldsymbol{c_\alpha})_{i_1}\cdots(\boldsymbol{c_\alpha})_{i_n}$ is split into $\Delta^{(n)}$, which is an isotropic tensor and $\Delta_{ij}^{(2)} = \delta_{ij}^{(2)}$, $\delta_{ijklpq}^{(6)}$ and $\Delta_{ijkl}^{(4,2)}$, are deviatoric, non-isotropic tensors. The detailed description of construction of isotropy lattice is given in [25] and expressions are given in Appendix A. In order to derive correction terms for D1Q3, D2Q9, D3Q15, D3Q19 and D3Q27 models, third-order moment of discrete distribution function is derived as follows:

$$\begin{aligned}
\sum_{\alpha=0}^{Q} f_\alpha^{eq}\mathcal{H}^{(3)}(\boldsymbol{\xi}) = \rho(1-\theta-u_iu_j)u_l\delta_{ijkl}\\
+ \rho u_iu_ju_k + \rho(RT-1)[u\delta]^{(3)}
\end{aligned} \tag{25}$$

for a lattice with $(Q+1)$ discrete velocities, where $[u\delta]^{(3)} = u_i\delta_{jk} + u_j\delta_{ik} + u_k\delta_{ij}$, and $\delta_{ijkl} = 1$ when $i = j = k = l$, otherwise $\delta_{ijkl} = 0$.

It is worth noting that a slight modification of the expression is required in the D3Q15 and D3Q19 cases in order to obtain the same third-order velocity moment of f^{eq} [18]. When these low-symmetry models are adopted, it can be found that $f^{(eq)}$ and $h^{(eq)}$ rigorously satisfy the zeroth-, first- and second-order velocity moment constraints. However, one can see there is a deviation with third-order velocity moments obtained by Hermite projection of the continuous Maxwell–Boltzmann distribution.

This deviation for third-order velocity moment originates in the low-symmetry of the these lattice models and cannot be removed by choosing different equilibrium distribution functions. A natural remedy is to restore the missing cubic terms by correcting the third-order moment. Considering the orthogonality of Hermite polynomials 1, $\boldsymbol{\xi_i}$, $\boldsymbol{\xi_i\xi_j} - \delta_{ij}$, this is done by adding the following external force in the density distribution equation:

$$\frac{\partial f_\alpha}{\partial t} + \boldsymbol{\xi_\alpha}\cdot\frac{\partial f_\alpha}{\partial \boldsymbol{x}} = -\frac{1}{\tau_f}(f_\alpha - f_\alpha^{eq}) + \Phi_\alpha \tag{26}$$

with

$$\Phi_\alpha = \frac{9w_\alpha}{2}\left[\left(\xi_{\alpha_i}^2 - \frac{1}{3}\right)\phi_i\right] \tag{27}$$

where

$$\phi_i = \frac{\partial}{\partial x_i}[\rho(1-\theta-u_ku_k)u_i] \tag{28}$$

The gradient operator is implemented by the second-order centered finite differences.

In order to enhance stability of energy conservation equation and improve positivity of energy distribution function, the same correction approach on energy evolution equation is introduced with the correction term $\psi_i = \frac{\partial}{\partial x_i}(pRT)$. The higher-order term $p\theta\delta$ in Hermite expansion coefficient $\boldsymbol{b}_0{}^2$ is recovered by adding a correction term in energy evolution equation. The energy distribution function equation is modified as follows with $\Psi_\alpha = 3(\xi_{\alpha_i}\psi_i)$:

$$\frac{\partial h_\alpha}{\partial t} + \boldsymbol{\xi_\alpha}\cdot\frac{\partial h_\alpha}{\partial \boldsymbol{x}} = -\frac{1}{\tau_h}(h_\alpha - h_\alpha^{eq}) - \frac{1}{\tau_{hf}}(h'_\alpha) + \Psi_\alpha \tag{29}$$

A physical consistency constraint is that truncated approximation of equilibrium distribution functions should remain positive. The use of truncated expressions does not ensure a priori that positivity is preserved, and the robustness of the method is tied to the capability of a given truncated expression to remain positive in a wide range of flow configurations. For the sake of investigation of positivity preservation, one-dimensional density and total energy equilibrium distribution function have been studied for searching positive regions in the (Mach number – temperature) plane, while considering a constant density. In the analysis, the Mach number is defined as $Ma = u/\sqrt{RT_0}$ and temperature is calculated from $T = \theta T_0$.

The following equilibrium density and energy distribution functions are considered:

$$f_\alpha^{eq,1} = \omega_\alpha(\xi_\alpha, T_0)\rho\left\{1 + \frac{\xi_\alpha u}{RT_0} + \frac{1}{2}\left(\frac{\xi_\alpha u}{RT_0}\right)^2 - \frac{u^2}{2RT_0} + \frac{\theta-1}{2}\left(\frac{{\xi_\alpha}^2}{RT_0} - D\right) + \frac{\xi_\alpha u}{6RT_0}\left[\left(\frac{\xi_\alpha u}{RT_0}\right)^2 - \frac{3u^2}{RT_0} + 3(\theta-1)\left(\frac{{\xi_\alpha}^2}{RT_0} - D - 2\right)\right]\right\} \tag{30}$$

$$f_\alpha^{eq,2} = \omega_\alpha(\xi_\alpha, T_0)\rho\left\{1 + \frac{\xi_\alpha u}{RT_0} + \frac{1}{2}\left(\frac{\xi_\alpha u}{RT_0}\right)^2 - \frac{u^2}{2RT_0}\right\} \tag{31}$$

$$h_\alpha^{eq,1} = E f_\alpha^{eq,2} + \omega_\alpha(\xi_\alpha, T_0)p\left[\frac{\xi_\alpha u}{RT_0} + \left(\frac{\xi_\alpha u}{RT_0}\right)^2 - \frac{u^2}{RT_0} + \frac{\theta}{2}\left(\frac{{\xi_\alpha}^2}{RT_0} - D\right)\right] \tag{32}$$

$$h_\alpha^{eq,2} = E f_\alpha^{eq,2} + \omega_\alpha(\xi_\alpha, T_0)p\left[\frac{\xi_\alpha u}{RT_0} + \left(\frac{\xi_\alpha u}{RT_0}\right)^2 - \frac{u^2}{RT_0}\right] \tag{33}$$

$$h_\alpha^{eq,3} = E f_\alpha^{eq,2} + \omega_\alpha(\xi_\alpha, T_0)p\left[\frac{\xi_\alpha u}{RT_0} + \left(\frac{\xi_\alpha u}{RT_0}\right)^2 - \frac{u^2}{RT_0} + \frac{1}{2}\left(\frac{{\xi_\alpha}^2}{RT_0} - D\right)\right] \tag{34}$$

$$h_\alpha^{eq,4} = E f_\alpha^{eq,1} + \omega_\alpha(\xi_\alpha, T_0)p\left[\frac{\xi_\alpha u}{RT_0} + \left(\frac{\xi_\alpha u}{RT_0}\right)^2 - \frac{u^2}{RT_0} + \frac{\theta}{2}\left(\frac{{\xi_\alpha}^2}{RT_0} - D\right)\right] \tag{35}$$

where $D = 1$, u is one-dimensional velocity and $\xi_\alpha = [-1, 0, 1]$, $\omega_\alpha(\xi_\alpha, T_0) = [1/3, 2/3, 1/3]$.

The total energy equilibrium distribution function Eq. (32) is derived from total energy equilibrium distribution function assuming that the density equilibrium distribution function is given by Eq. (31). Eq. (33) is derived from Eq. (32) equilibrium distribution function in which non-dimensional temperature is set equal $\theta = 0$. Eq. (34) is also obtained from equilibrium distribution function Eq. (32) in which non-dimensional temperature is taken equal to $\theta = 1$. The last total energy equilibrium distribution function Eq. (35) is obtained from total energy equilibrium distribution function assuming that the density equilibrium distribution function is given by Eq. (30).

The positive region of density equilibrium distribution function, i.e. $f_\alpha^{eq} \geq 0$ and the energy distribution function, i.e. $h_\alpha^{eq} \geq 0$, are then sought for by exploring the (*Ma, T*) plane.

Fig. 1 shows the positive region of density equilibrium distribution function Eq. (30) used in compressible flow, along with the positive region of Eq. (31) which is used for incompressible flow as a comparison. Considering $T = T_0$ for incompressible case, the positive region of Eq. (31) is just one vertical line of positive region of Eq. (30). Fig. 2 displays the positive regions of total energy equilibrium distribution functions $h^{eq,1}$-$h^{eq,4}$. It is observed that Eq. (33) exhibits the largest positive region along with Mach number and temperature. Thus, Eq. (33) is adopted as total energy equilibrium distribution function with correction term in this paper.

The macroscopic governing equations derived using Champman–Enskog expansion with cubic correction terms are derived in detail in Appendix B.

2.2. Time integration and spatial discrete scheme

In this paper, a finite-volume scheme, so-called DUGKS (discrete unified gas-kinetic scheme), is adopted for time integration and spatial discretization which is firstly proposed by Guo et al. [26,27]. The DUGKS has the asymptotic preserve (AP) property in capturing Navier-Stokes solutions. Due to the features of finite volume scheme, it could be simply and naturally used on non-uniform and unstructured irregular meshes. Moreover, DUGKS releases the close coupling of discrete micro-velocities and temporal/spatial discretization. In the contrary, the temporal and spatial discretization is associated with the discrete micro-velocites by regular lattices in LBM. Furthermore, DUGKS overcomes the defects of conventional FV-LBM methods, such as large numerical dissipation, and poor numerical stability. The detailed discussion and comparison is presented in [26–28].

Integrating Eqs. (1) and (2) from time t_n to $t_{n+1} = t_n + \Delta t$, one obtains

$$f(x, t_{n+1}) = f(x, t_n) - \frac{\Delta t}{V}F^{n+1/2} + \frac{\Delta t}{2}(\Omega_{n+1} + \Omega_n) \tag{36}$$

$$h(x, t_{n+1}) = h(x, t_n) - \frac{\Delta t}{V}H^{n+1/2} + \frac{\Delta t}{2}(\Omega_{n+1} + \Omega_n) \tag{37}$$

where $F^{n+1/2} = \int_{\partial V}(\boldsymbol{\xi}\cdot\boldsymbol{n})f(x, t_{n+1/2})d\boldsymbol{S}$, $H^{n+1/2} = \int_{\partial V}(\boldsymbol{\xi}\cdot\boldsymbol{n})h(x, t_(n+1/2))d\boldsymbol{S}$ and $\boldsymbol{n}$ is unit normal. The midpoint rule for the integration of convective term and the trapezoidal rule for the collision term is used. In order to remove this implicit treatment of the collision term, the new distribution functions are introduced: $\tilde{f} = f - \Delta t/2\Omega$, $\tilde{f^+} = f + \Delta t/2\Omega$, $\tilde{h} = h - \Delta t/2\Omega$, and $\tilde{h^+} = h + \Delta t/2\Omega$. Thus Eqs. (36) and (37) can be rewritten as

$$\tilde{f}(x, t_{n+1}) = \tilde{f^+}(x, t_n) - \frac{\Delta t}{V}F^{n+1/2} \tag{38}$$

$$\tilde{h}(x, t_{n+1}) = \tilde{h^+}(x, t_n) - \frac{\Delta t}{V}H^{n+1/2} \tag{39}$$

The evaluation of the gas density distribution function f and total energy distribution function h at the cell interfaces is a key issue in the finite volume scheme. The same reconstruction operator with DUGKS is employed in this study to calculate variables at interface between neighboring mesh cells. However, one of the key differences between the present method and DUGKS is that a total energy distribution function is adopted for energy conservation equation rather than BGK–Shakhov model.

The distribution functions at interface are reconstructed using the following formula:

$$f_\alpha(x_f, \boldsymbol{\xi_\alpha}, t + 1/2\Delta t) = f_\alpha(x_f, \boldsymbol{\xi_\alpha}, t) - 1/2\Delta t\boldsymbol{\xi_\alpha}\cdot\boldsymbol{\sigma_{f_\alpha}} \tag{40}$$

$$h_\alpha(x_f, \boldsymbol{\xi_\alpha}, t + 1/2\Delta t) = h_\alpha(x_f, \boldsymbol{\xi_\alpha}, t) - 1/2\Delta t\boldsymbol{\xi_\alpha}\cdot\boldsymbol{\sigma_{h_\alpha}} \tag{41}$$

The gradient $\sigma_{f_\alpha} = \nabla f_\alpha(x_f, \boldsymbol{\xi_\alpha}, t)$ and $\sigma_{h_\alpha} = \nabla h_\alpha(x_f, \boldsymbol{\xi_\alpha}, t)$ can be approximated by linear interpolation reconstructions. In this paper, the slope σ in each cell is reconstructed from cell-averaged

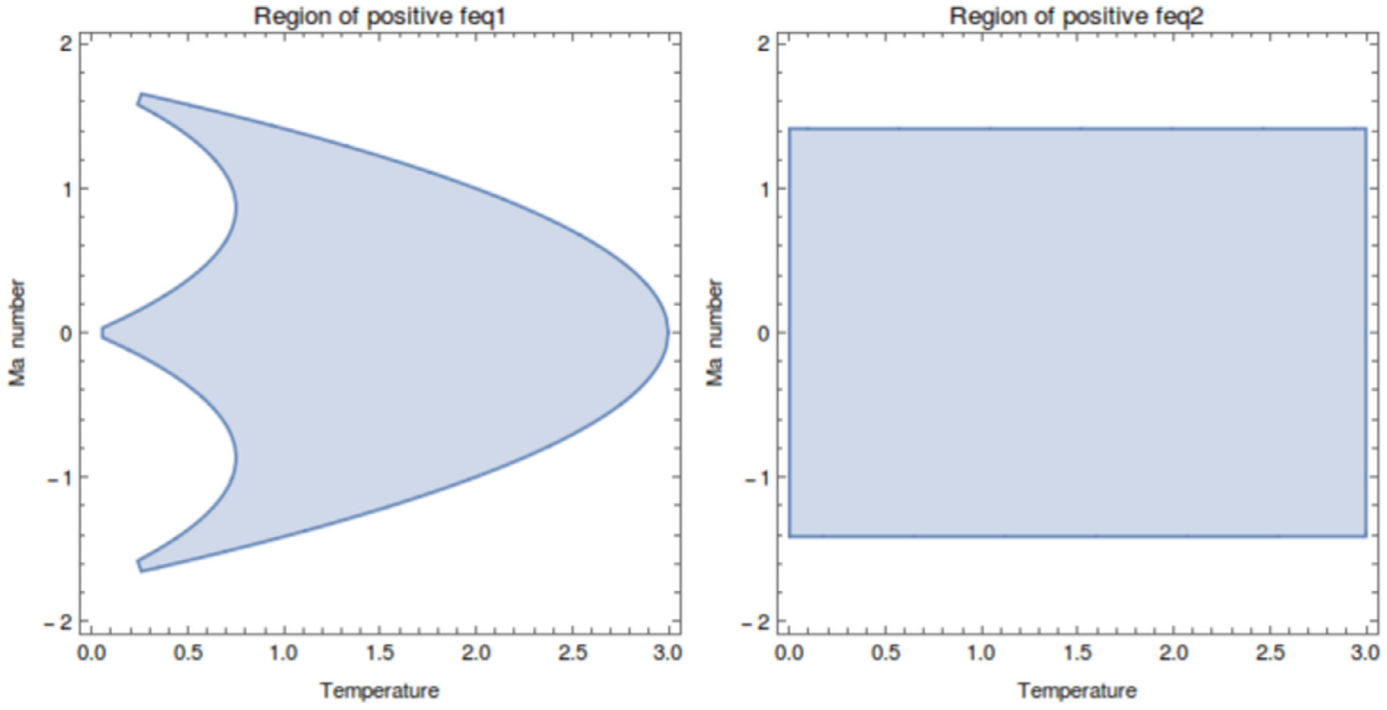

Fig. 1. Positivity of density equilibrium function $f^{eq,1}$ (left) and $f^{eq,2}$ (right).

values using some numerical limiters in order to allow for shock capturing. The van Leer limiter is adopted

$$\sigma = [sgn(s_1) + sgn(s_2)]\frac{|s_1||s_2|}{|s_1| + |s_2|}$$
$$s_1 = \frac{\phi_j - \phi_{j-1}}{x_j - x_{j-1}}, s_2 = \frac{\phi_{j+1} - \phi_j}{x_{j+1} - x_j}, \tag{42}$$

In order to calculate gas density distribution function f and total energy distribution function h of midpoint time step at the cell interfaces, several intermediate distribution functions are employed in evolution process of density and total energy distribution functions. Those intermediate distribution functions can be derived from f_α, f_α^{eq} and h_α, h_α^{eq} located at cell and cell interface, refer to [26].

The macroscopic density ρ, velocity $\boldsymbol{u}$ and total energy E at cell interface x_f can be obtained from distribution functions using the classical reconstruction formula, rather than interpolating them:

$$\rho(x_f, t) = \sum_{\alpha=0}^{Q} f_\alpha(x_f, \boldsymbol{\xi_\alpha}, t)$$
$$\rho(x_f, t)\boldsymbol{u}(x, t) = \sum_{\alpha=0}^{Q} \boldsymbol{\xi_\alpha} f_\alpha(x_f, \boldsymbol{\xi_\alpha}, t)$$
$$E(x_f, t) = \sum_{\alpha=0}^{Q} h_\alpha(x_f, \boldsymbol{\xi_\alpha}, t) \tag{43}$$

It is worth pointing out that there are some key differences among the present model, DUGKS and standard LBM for simulation of thermal compressible flow. Firstly, the regular discrete velocities of LBM are adopted in the present model. The number of discrete velocities of the present model is much smaller than one in DUGKS. This feature will lead to a better computational efficiency than DUGKS. Moreover, the equilibrium density and total energy distribution functions are in the form of third- and second-order truncated Hermite polynomials rather than higher order Hermite polynomials or Newton–Cotes polynomials. Comparing with standard LBM, the present model can recover fully compressible Navier–Stokes–Fourier equations with equation of state for perfect gas on the same regular discrete velocities. The finite volume scheme with an asymptotic preserve property enable it has good numerical stability and small numerial dissipation.

3. Numerical tests and results

In this section, several numerical simulations including Sod shock tube, thermal compressible Couette flow and two-dimensional Riemann problem are carried out for assessing the present model in compressible thermal flows.

3.1. Sod shock tube

Firstly, a standard test case of compressible flow is the shock tube problem. The flow of the Riemann problem includes a shock wave, a contact surface, and an expansion wave. Therefore, it is a very relevant test case to study the performance of the numerical schemes in simulation of compressible flows. Sod shock tube test is considered with the initial condition as follows:

$$\left(\frac{\rho}{\rho_0}, \frac{u}{u_0}, \frac{p}{p_0}\right) = (1, 0, 1), 0 < \frac{x}{L} < \frac{1}{2}$$
$$\left(\frac{\rho}{\rho_0}, \frac{u}{u_0}, \frac{p}{p_0}\right) = (0.125, 0, 0.1), \frac{1}{2} < \frac{x}{L} < 1 \tag{44}$$

The periodical condition was taken in the y direction and $f_\alpha = f_\alpha^{eq}$ is set in the x direction. The specific heat ratio is $\gamma = 1.4$ and the Prandtl number is 1.0. The simulations are performed on three grid numbers (100, 200, 400). As conducted in Appendix B, the governing equations derived by the present method are compressible Navier–Stokes equations. In order to obtain an approximated solution of Euler equations, a small viscosity of 10^{-5} is given in the case. A typical situation is shown in Fig. 3. The profiles of the density, velocity, pressure and temperature for Sod shock tube obtained from the simulations are presented. The theoretical solution is represented with solid points for comparison in the figure. The

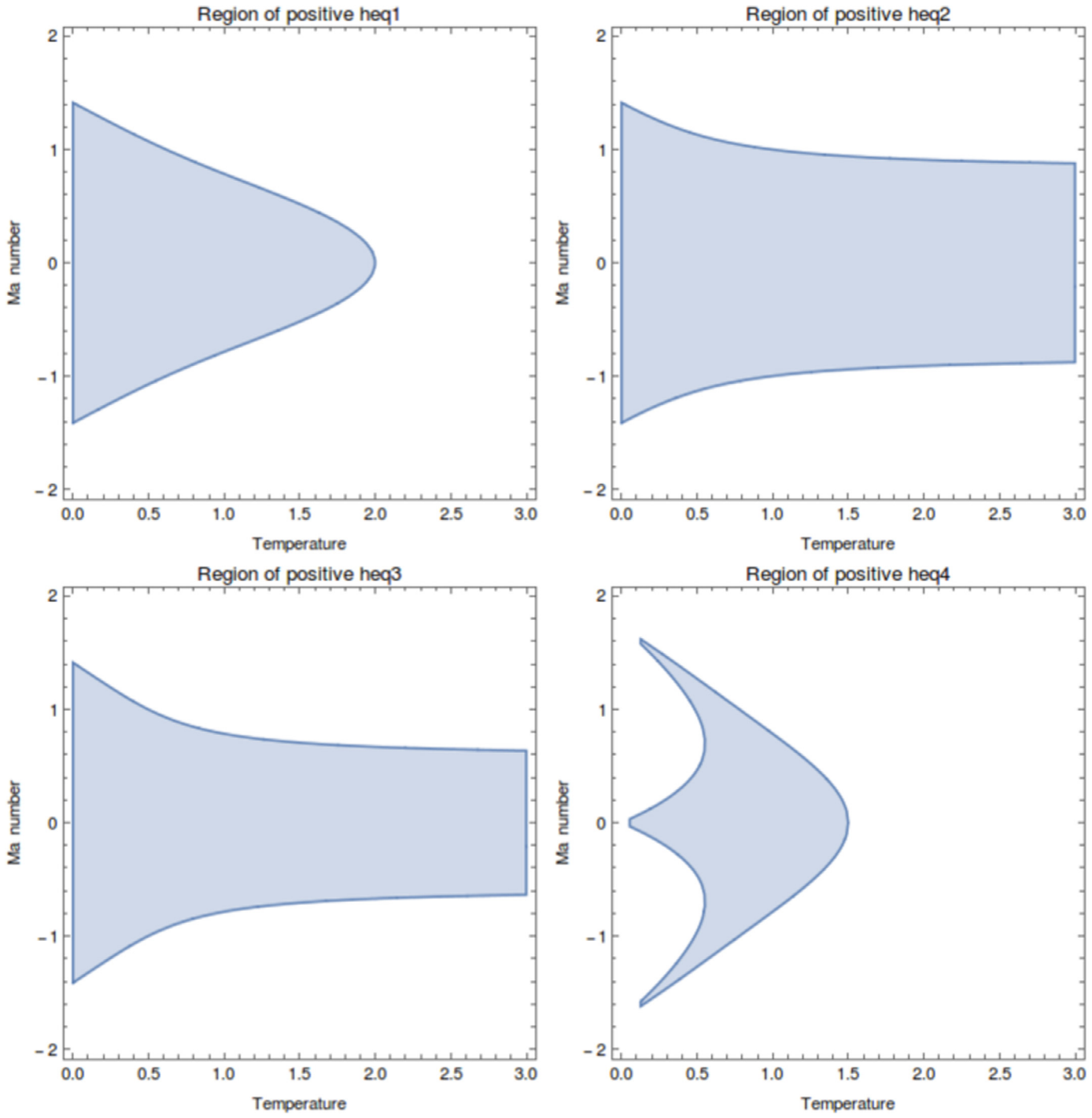

Fig. 2. Positivity of energy equilibrium function $h^{eq,1}$ (top, left), $h^{eq,2}$ (top, right), $h^{eq,3}$ (bottom, left), $h^{eq,4}$ (bottom, right) .

reference values obtained using discrete unified gas kinetic scheme on a 100 grid with 201 discrete velocities is also drawn in the figures. The numerical results are found to be in an excellent agreement with the theoretical ones. It is noted that the discontinuities were captured exactly. With the increasing of mesh resolution from 100 to 400, the results show a considerable improvement. The profiles obtained by the present method on 200 nodes with only three regular discrete velocities are quite close to those calculate by DUGKS on a 100 grid with 201 discrete velocities.

Moreover, the accuracy of the present method and conventional CFD solver is evaluated by comparing their density profiles and temperature profiles at different grid numbers and with or without physical viscosity. In conventional CFD solver, flux vector splitting (FVS) is used to obtain convective flux. The third-order MUSCL (monotone upstream-centered schemes for conservation laws) scheme is employed to reconstruct variables on the faces. And the transient term is advanced by the third-order Runge–Kutta scheme [29]. Fig. 4 shows that all of the results are reliable and accurate, compared with analytical solution. “MUSCL-NS-400” and “MUSCL-NS-200” represent results solved by the third-order CFD solver at a small viscosity of 10^{-5} on 400 and 200 uniform grids, respectively. And the results obtained by the third-order Euler solver on 400 uniform grids are denoted by “MUSCL-EULER-400”. “LBM-400” stands for density profile and

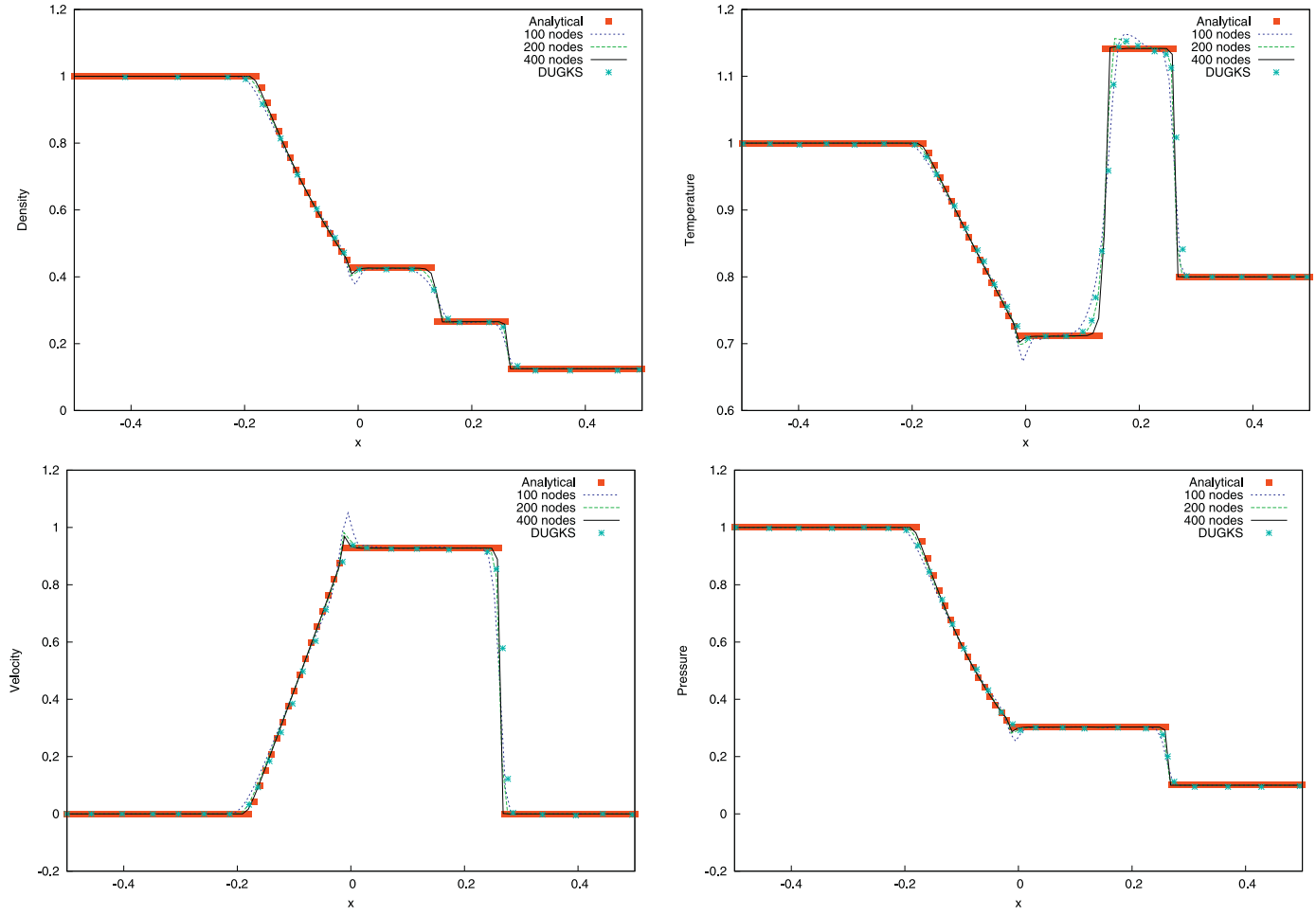

Fig. 3. Numerical solutions of Sod shock tube. density (top, left), temperature (top, right), velocity (bottom, left), pressure (bottom, right).

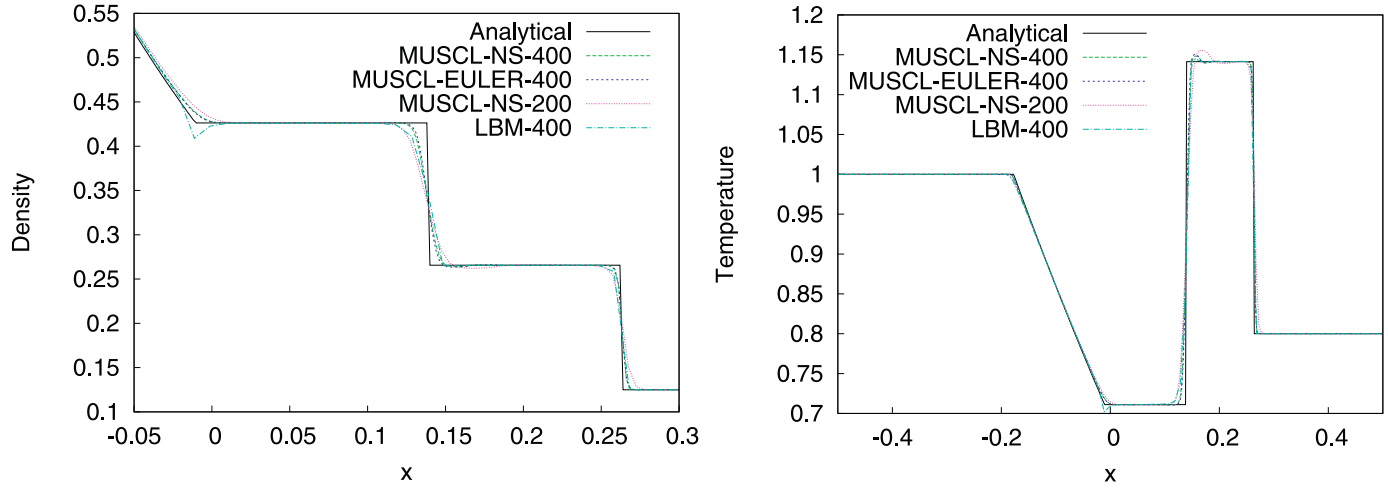

Fig. 4. Comparison of solutions between CFD and LBM. density (left), temperature (right).

temperature profile calculated by the present method at a small viscosity of 10^{-5} on 400 uniform grids. It can be found that the results of LBM fall in between those on 400 grids and those on 200 grids by third-order CFD method. Besides, the Navier–Stokes solution at small viscosity is confirmed closely to solution of Euler equations.

3.2. Thermal Couette flow

In this section, thermal Couette flow between two parallel plates is considered to assess capability of the present model being able to capture viscous heat dissipation. Considering the viscous fluid flow between two infinite parallel plates, the lower plate is

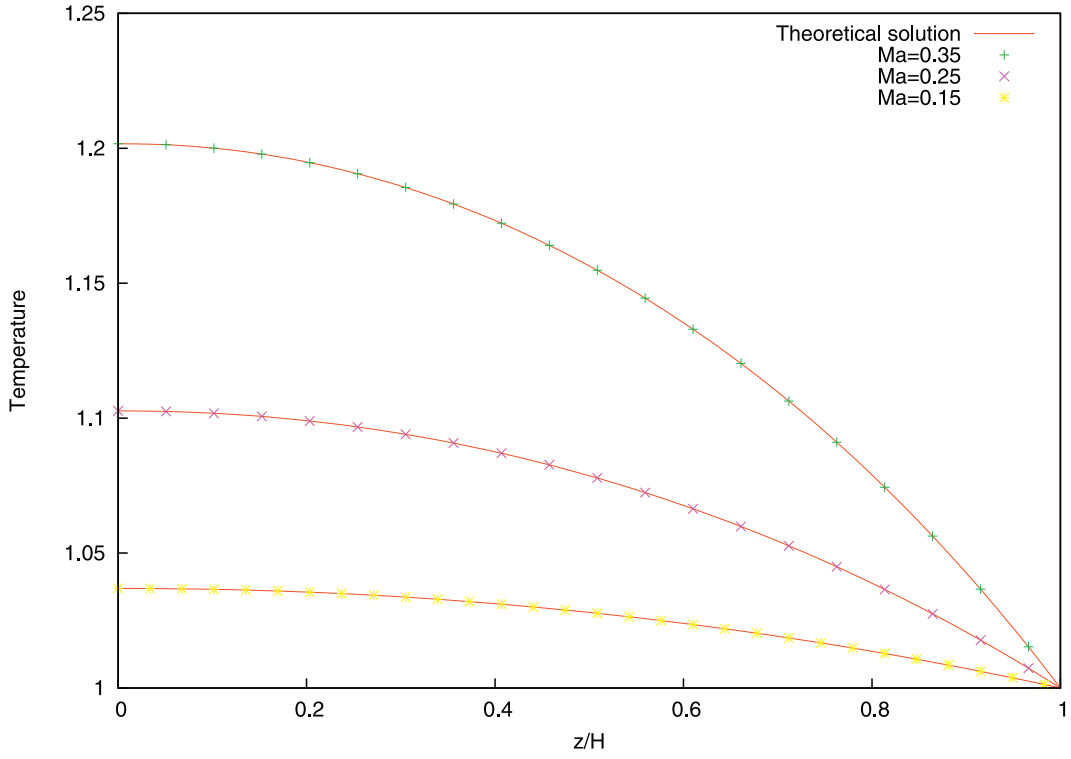

Fig. 5. Temperature profiles for $Ma = 0.15, 0.25$ and 0.35, $Pr = 5$, $Ma = U/\sqrt{\gamma RT_0}$.

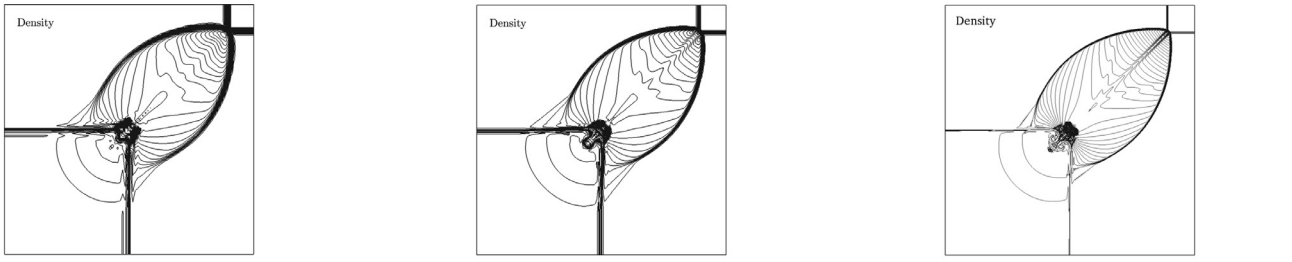

(a) Density distribution on 100×100 grids (b) Density distribution on 200×200 grids (c) Density distribution on 400×400 grids

Fig. 6. Density distribution of 2D Riemann problem.

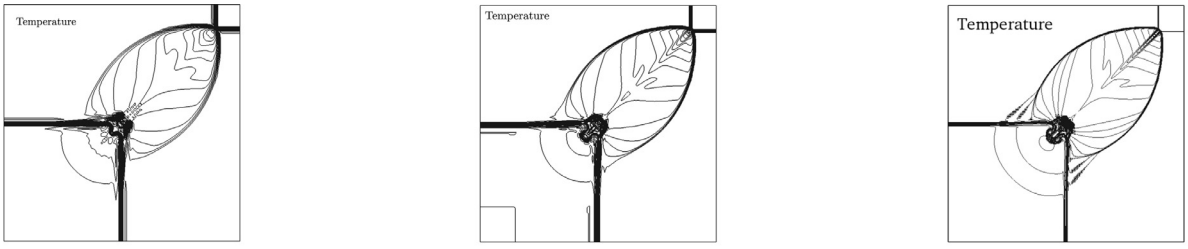

(a) Temperature contours on 100×100 grids (b) Temperature contours on 200×200 grids (c) Temperature contours on 400×400 grids

Fig. 7. Temperature contours of 2D Riemann problem.

fixed and the upper one is moving at speed U. The viscous shear stress transfers momentum and viscous heat dissipation into the fluid. Thus, it modifies both the horizontal speed profile and temperature profile. The ratio $Pr = \mu c_v/\lambda$ is assumed to be constant, which is reasonable for a perfect gas. Assuming that $\mu/\mu_0 = T/T_0$ and that the lower wall is adiabatic, an analytical solution can be found [22,30]:

$$\frac{T(y)}{T_0} = 1 + A\left[1 - \left(\frac{u(y)}{U}\right)^2\right] \tag{45}$$

$$\left(1 + \frac{2}{3}A\right)\frac{y}{H} = \frac{u(y)}{U} + A\left[\frac{u(y)}{U} - \frac{1}{3}\left(\frac{u(y)}{U}\right)^3\right] \tag{46}$$

where H refers to the distance between the two plates and

$$A = Pr\frac{\gamma - 1}{2}Ma^2 \tag{47}$$

Fig. 5 displays dimensionless temperature profiles for $Ma = 0.15$, 0.25 and 0.35 with $Pr = 5$. The results for all cases exactly agree with the analytical value, showing the high accuracy of the proposed model. It can be found that the heat dissipation play

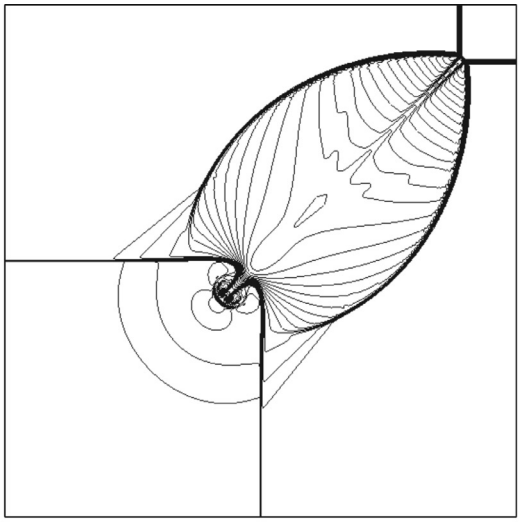

(a) Density distribution on 400 × 400 grids by the 3rd CFD

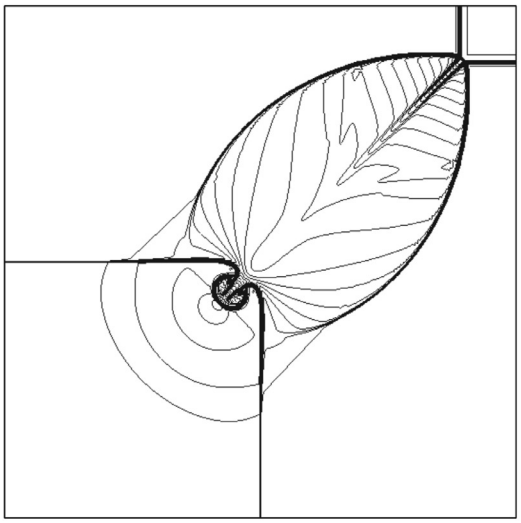

(b) Temperature distribution on 400 × 400 grids by the 3rd CFD

Fig. 8. Density distribution of 2D Riemann problem.

more important role in the thermal Coutte flow when Mach number increases. The present method has a good capability to capture the thermal compressible phenomena.

3.3. Two dimensional Riemann problem

In two dimensional Riemann problem, the computational domain is a square of length 1 and height 1. The computational domain is uniformly divided into 100 × 100, 200 × 200 and 400 × 400 Cartesian grids. A typical configuration is considered in this test as following initial condition [31]:

$$\begin{aligned}
\left(\frac{\rho}{\rho_0}, \frac{u}{u_0}, \frac{v}{v_0}, \frac{p}{p_0}\right) &= (0.531, 0, 0, 0.4), \frac{1}{2} < \frac{x}{L} < 1, \frac{1}{2} < \frac{y}{L} < 1 \\
\left(\frac{\rho}{\rho_0}, \frac{u}{u_0}, \frac{v}{v_0}, \frac{p}{p_0}\right) &= (1, 0.7276, 0, 1), 0 \le \frac{x}{L} \le \frac{1}{2}, \frac{1}{2} < \frac{y}{L} < 1 \\
\left(\frac{\rho}{\rho_0}, \frac{u}{u_0}, \frac{v}{v_0}, \frac{p}{p_0}\right) &= (0.8, 0, 0, 1), 0 \le \frac{x}{L} \le \frac{1}{2}, 0 \le \frac{y}{L} \le \frac{1}{2} \\
\left(\frac{\rho}{\rho_0}, \frac{u}{u_0}, \frac{v}{v_0}, \frac{p}{p_0}\right) &= (1, 0, 0.7276, 1), \frac{1}{2} < \frac{x}{L} < 1, 0 \le \frac{y}{L} \le \frac{1}{2}
\end{aligned} \tag{48}$$

The flow computed by the present model is displayed in Figs. 6 and 7. As can be seen from figures the results of density and temperature distributions are well calculated by the present model. The complex flow features with shock wave are accurately captured. In order to compare our results with those obtained by shock capturing scheme in the framework of conventional CFD methods, the problem is also solved by FVS with the third-order MUSCL scheme and the third-order Runge-Kutta scheme for time marching [29]. Fig. 8 shows the density and temperature distributions solved by the conventional CFD method. The results obtained by the proposed model are closely consistent with with those obtained by using the shock capturing scheme on 400 × 400 uniform grids. It can be noticed that the proposed model shows good performance on multi-dimensional simulation due to its orthogonality feature.

4. Conclusion

A multi-dimensional double distribution function thermal lattice Boltzmann model for fully compressible flows has been developed in this paper. A finite volume scheme has been adopted as a temporal and spatial discrete scheme. The third-order density equilibrium distribution functions and second order total energy equilibrium distribution functions are developed and studied on regular lattice. Cubic correction terms have been derived using orthogonality of Hermite polynomials to recover fully compressible Navier–Stokes–Fourier equations without cubic defects. Numerical simulations for Sod shock tube, thermal Couette flows and two-dimensional Riemann problem have shown that the present model can easily handle compressible flows at moderate Mach number and thermal compressible flows with viscous heat dissipation and pressure work.

Acknowledgement

This work was performed under support by the National Natural Science Foundation of China (51136004) and China Scholarship Council.

Appendix A. Lattice tensor

There is D2Q9 lattice model for two-dimensional model, and there are three common discrete velocity models, namely the fifteen-velocity model (D3Q15), the nineteen-velocity model (D3Q19) and the twenty-seven-velocity model (D3Q27) three-dimensional lattices for three-dimensional simulation. They are shown in Table B.1.

In Table B.1, the lattice tensor $\boldsymbol{E}^{(n)} = \sum_{\alpha} (\boldsymbol{c}_{\boldsymbol{\alpha}})_{i_1} \cdots (\boldsymbol{c}_{\boldsymbol{\alpha}})_{i_n}$ is split into $\Delta^{(n)}$, which is an isotropic tensor and $\Delta^{(2)}_{ij} = \delta^{(2)}_{ij}$, $\delta^{(6)}_{ijklpq}$ and $\Delta^{(4,2)}_{ijkl}$, are deviatoric, non-isotropic tensors.

Appendix B. Hydrodynamic limit of thermal compressible model

In hydrodynamic limit, we apply the Chapman–Enskog multiscale technique to derive macroscopic equations. Taking into account that the equilibrium density distribution function satisfies the velocity moment condition to recover the compressible macroscopic Navier–Stokes equations, the distribution functions f_α and

Table B1
Discrete velocities and corresponding weights.

Velocities $\boldsymbol{C}_\alpha$	Weights	N	$E_{ij}^{(2)}$	$E_{ijkl}^{(4)}$	$E_{ijklpq}^{(6)}$
Discrete model D2Q9					
(0, 0)	4/9	1	0	0	0
cyc (± 1, 0)	1/9	4	$2\delta_{ij}$	$2\delta_{ijlk}$	$2\delta_{ijlkpq}$
(± 1, ± 1)	1/36	4	$4\delta_{ij}$	$4\Delta_{ijkl}^{(4)} - 8\delta_{ijlk}$	Π_{bc}^{2D}
Discrete model D3Q15					
(0, 0, 0)	2/9	1	0	0	0
cyc (± 1, 0, 0)	1/9	6	$2\delta_{ij}$	$2\delta_{ijlk}$	$2\delta_{ijlkpq}$
(± 1, ± 1, ± 1)	1/72	8	$8\delta_{ij}$	$8\Delta_{ijkl}^{(4)} - 16\delta_{ijlk}$	Π_{bc}
Discrete model D3Q19					
(0, 0, 0)	1/3	1	0	0	0
cyc (± 1, 0, 0)	1/18	6	$2\delta_{ij}$	$2\delta_{ijlk}$	$2\delta_{ijlkpq}$
cyc (± 1, ± 1, 0)	1/36	12	$8\delta_{ij}$	$4\Delta_{ijkl}^{(4)} - 4\delta_{ijlk}$	Π_{fc}
Discrete model D3Q27					
(0, 0, 0)	8/27	1	0	0	0
cyc (± 1, 0, 0)	2/27	6	$2\delta_{ij}$	$2\delta_{ijlk}$	$2\delta_{ijlkpq}$
cyc (± 1, ± 1, 0)	1/54	12	$8\delta_{ij}$	$4\Delta_{ijkl}^{(4)} - 4\delta_{ijlk}$	Π_{fc}
(± 1, ± 1, ± 1)	1/216	8	$8\delta_{ij}$	$8\Delta_{ijkl}^{(4)} - 16\delta_{ijlk}$	Π_{bc}

Note1: $\Pi_{bc}^{2D} = 4/3\Delta_{ijkl}^{(4.2)} - 16\delta_{ijlkpq}$

Note2: $\Pi_{fc} = 4(\Delta_{ijkl}^{(4.2)} - 13\delta_{ijlkpq})$, $\Pi_{bc} = 8(\Delta_{ijklpq}^{(6)} - 2\Delta_{ijkl}^{(4.2)} + 16\delta_{ijlkpq})$

h_α are expanded around the f_α^{eq} and $h_\alpha{}^{eq}$ distributions as follows:

$$f_\alpha = f_\alpha^{(0)} + f_\alpha^{(1)} \tag{B.1}$$

$$h_\alpha = h_\alpha^{(0)} + h_\alpha^{(1)} \tag{B.2}$$

By inserting the expanded functions in the lattice Boltzmann equation, one obtains

$$\left(\frac{\partial}{\partial t_1} + \boldsymbol{\xi}_\alpha \cdot \nabla_1\right) f_\alpha^{eq} = -\frac{f_\alpha^{(1)}}{\tau_f} \tag{B.3}$$

and

$$\left(\frac{\partial}{\partial t_1} + \boldsymbol{\xi}_\alpha \cdot \nabla_1\right) h_\alpha^{eq} = -\frac{h_\alpha^{(1)}}{\tau_h} \tag{B.4}$$

Computing the zeroth- and first-order moment of Eqs. (B.3) and (B.4) in the velocity phase space, one obtains the following continuity equation, momentum equation and energy conservation:

$$\frac{\partial \rho}{\partial t} + \frac{\partial}{\partial x_j}(\rho u_j) = 0 \tag{B.5}$$

$$\frac{\partial}{\partial t}(\rho u_i) + \frac{\partial}{\partial x_j}(\rho u_i u_j + p\delta_{ij}) = 0 \tag{B.6}$$

$$\frac{\partial \rho E}{\partial t} + \frac{\partial}{\partial x_j}[(\rho E + p)u_j] = 0 \tag{B.7}$$

where $p = \rho RT$ is the equation of state.

Combining Eqs. (B.5) and (B.6), one can obtain

$$\partial_t(\rho u_i u_j) = -u_i \partial_j p - u_j \partial_i p - \partial_k(\rho u_i u_j u_k) \tag{B.8}$$

Combining Eqs. (B.7) and (B.6), one can obtain

$$\partial_t p = -\partial_k(p u_k) - \frac{2}{b} p \partial_k u_k \tag{B.9}$$

The stress tensor and heat flux can be decomposed into their Chapman–Enskog counterparts:

$$\boldsymbol{P} = \boldsymbol{P}^{(0)} + \boldsymbol{P}^{(1)} = \rho RT\boldsymbol{I} + \boldsymbol{P}^{(1)}, \boldsymbol{q} = \boldsymbol{q}^{(0)} + \boldsymbol{q}^{(1)}. \tag{B.10}$$

where $\boldsymbol{P}^{(1)}$ and $\boldsymbol{q}^{(1)}$ represent non-equilibrium stress tensor and heat flux, respectively. Following the standard procedure, we can expand the off-equilibrium distribution function $f^{(1)}$ and $h^{(1)}$ in terms of Hermite polynomials:

$$f^{(1)} = \omega(\boldsymbol{\xi}, T)\sum_{n=0}^{N} \frac{1}{n!}\boldsymbol{a}_1^{(n)}\mathcal{H}^{(n)}(\boldsymbol{\xi}) \tag{B.11}$$

$$h^{(1)} = \omega(\boldsymbol{\xi}, T)\sum_{n=0}^{N} \frac{1}{n!}\boldsymbol{b}_1^{(n)}\mathcal{H}^{(n)}(\boldsymbol{\xi}) \tag{B.12}$$

Owing to orthogonality of Hermite polynomials, $\boldsymbol{P}^{(1)}$ and $\boldsymbol{q}^{(1)}$ can be easily obtained in terms of Hermite coefficients:

$$P_{ij}^{(1)} = a_{1,ij}^{(2)}, \quad q_i^{(1)} = b_{1i}^{(1)}. \tag{B.13}$$

Here, we project Eqs. (B.3) and (B.4) on Hermite basis:

$$\partial_t \boldsymbol{a}_0^{(2)} + \nabla \cdot \boldsymbol{a}_0^{(3)} + (\nabla \boldsymbol{a}_0^{(1)} + perm) - \boldsymbol{\Phi}^{(2)} = -\frac{1}{\tau_f}\boldsymbol{a}_1^{(2)} \tag{B.14}$$

$$\partial_t \boldsymbol{b}_0^{(1)} + \nabla \cdot \boldsymbol{b}_0^{(2)} + (\nabla \boldsymbol{b}_0^{(0)} + perm) - \boldsymbol{\Psi}^{(12)} = -\frac{1}{\tau_h}\boldsymbol{b}_1^{(1)} \tag{B.15}$$

where *perm* represents permutation of tensor $\nabla \boldsymbol{a}_0^{(1)}$ or $\nabla \boldsymbol{b}_0^{(0)}$. Using $\boldsymbol{\Phi}$ in Eq. (B.14), one obtains

$$\begin{aligned}
-\frac{1}{\tau_f}\boldsymbol{a}_1^{(2)} &= -u_i\partial_j p - u_j\partial_i p - \partial_k\left(\rho u_i u_j u_k\right) + \partial_t\left(p\delta_{ij}\right) - \partial_t\left(\rho\delta_{ij}\right) \\
&\quad + \partial_k\left[p\left(u_k\delta_{ij} + u_j\delta_{ik} + u_i\delta_{jk}\right)\right] + \partial_j\rho u_i + \partial_i\rho u_j \\
&= -u_i\partial_j p - u_j\partial_i p - \partial_k\left(\rho u_i u_j u_k\right) - \frac{2}{D}p\partial_k u_k - \partial_k\left(p u_k\delta_{ij}\right) \\
&\quad + \partial_k\left(\rho u_k\delta_{ij}\right) + \partial_i\left(p u_j\right) + \partial_j\left(p u_i\right) + \partial_k\left(p u_k\delta_{ij}\right) \\
&\quad - \partial_i\left(\rho u_j\right) - \partial_j\left(\rho u_i\right) - \partial_k\left(\rho u_k\delta_{ij}\right) + \partial_i\left(\rho u_j\right) + \partial_j\left(\rho u_i\right) \\
&= p\left(\partial_i u_j + \partial_j u_i\right) - \partial_k\left(\rho u_i u_j u_k\right) - \frac{2}{D}p\partial_k u_k\delta_{ij} \\
&= p\left(\partial_i u_j + \partial_j u_i\right) - \frac{2}{D}p\partial_k u_k\delta_{ij}
\end{aligned} \tag{B.16}$$

Using $\boldsymbol{\Psi}$ in Eq. (B.15), One can obtain

$$\begin{aligned}
-\frac{1}{\tau_h}\boldsymbol{b}_1^{(1)} &= \partial_t[p + \rho E\boldsymbol{u}] + \nabla\cdot[(2p + \rho E)\boldsymbol{u}\boldsymbol{u} \\
&\quad + [0 \times pRT + \rho E(RT - 1)]\delta] \\
&\quad + \nabla((p + \rho E)\boldsymbol{u}) - \boldsymbol{\Psi} - \boldsymbol{u}\frac{\boldsymbol{a}_1^{(2)}}{\tau_{hf}} \\
&= -(p + \rho E)u_i\partial_i u_j - \left(\frac{p}{\rho} + E\right)\partial_j p - u_j\partial_k[(\rho E + 2p)u_k] \\
&\quad + \partial_i[(2p + \rho E)u_i u_j + pRT\delta_{ij} + \rho E(RT - 1)\delta_{ij}] \\
&\quad - \frac{2}{D}p u_j\partial_k u_k + \partial_j\rho E - u_i\frac{a_{1ij}^{(2)}}{\tau_{hf}} \\
&= p u_i\partial_i u_j - (\frac{p}{\rho} + E)\partial_j p - \frac{2}{b}p u_j\partial_i u_i + \partial_j\left[\left(\frac{p}{\rho} + E\right)p\right] \\
&\quad - u_i\frac{a_{1ij}^{(2)}}{\tau_{hf}} \\
&= p\partial_j\left(\frac{p}{\rho} + c_v T + \frac{1}{2}u_i u_i\right) + p u_i\partial_i u_j - \frac{2}{b}p u_j\partial_i u_i - u_i\frac{a_{1ij}^{(2)}}{\tau_{hf}} \\
&= p(c_v + R)\partial_j T + p u_i\left(1 + \frac{\tau_f}{\tau_{hf}}\right)(\partial_i u_j + \partial_j u_i)
\end{aligned} \tag{B.17}$$

Using Eqs. (B.16) and (B.17), the following Navier–Stokes–Fourier equations are recovered:

$$\frac{\partial \rho}{\partial t} + \frac{\partial}{\partial x_j}(\rho u_j) = 0 \tag{B.18}$$

$$\frac{\partial}{\partial t}(\rho u_i) + \frac{\partial}{\partial x_j}\left(\rho u_i u_j + p\delta_{ij}\right) - \frac{\partial}{\partial x_j}\Pi_{ij} = 0 \tag{B.19}$$

$$\begin{aligned}\frac{\partial \rho E}{\partial t} &+ \frac{\partial}{\partial x_j}\left[(\rho E + p)u_j\right] - \frac{\partial}{\partial x_j}\left(\tau_h p(c_v + R)\partial_{x_j} T\right) \\ &+ \frac{\partial}{\partial x_j}\left(u_i \Pi_{ij}\right) = 0\end{aligned} \tag{B.20}$$

where pressure $p = \rho RT$ satisfies the equation of state for perfect gas, and the viscous stress tensor Π is given by

$$\Pi_{ij} = \tau_f p\left[\left(\frac{\partial u_i}{\partial x_j} + \frac{\partial u_j}{\partial x_i}\right) - \frac{2}{D}\frac{\partial u_k}{\partial x_k}\delta_{ij}\right] \tag{B.21}$$

The dynamic viscosity is defined as $\mu = \tau_f p$. The thermal conductivity is equal to $\lambda = \tau_h p(c_v + R)$ in energy conservation equation. Note that the Prandtl number of the present model is $Pr = \mu c_p/\lambda$, where $c_p = c_v + R$ is specific heat at constant pressure which can be adjusted in the present thermal lattice model.

References

[1] Qian Y, D'Humires D, Lallemand P. Lattice BGK models for Navier–Stokes equation. Europhys Lett 1992;17:479–84.
[2] Qian YH. Simulating thermo-hydrodynamics with lattice BGK models. J Sci Comput 1993;8:231–42.
[3] Chen SY, Doolen GD. Lattice Boltzmann method for fluid flows. Annu Rev Fluid Mech 1998;30:329–64.
[4] Succi S. The lattice Boltzmann equation: for fluid dynamics and beyond. In: Numerical mathematics and scientific computation. Oxford: Clarendon Press; 2001.
[5] Aidun CK, Clausen JR. Lattice-Boltzmann method for complex flows. Annu Rev Fluid Mech 2010;42:439–72.
[6] Lallemand P, Luo LS. Hybrid finite-difference thermal lattice Boltzmann equation. Int J Modern Phys B 2003;17:41–7.
[7] He XY, Chen SY, Doolen GD. A novel thermal model for the lattice Boltzmann method in incompressible limit. J Comput Phys 1998;146:282–300.
[8] Guo ZL, Zheng CG, Shi BC, Zhao TS. Thermal lattice Boltzmann equation for low mach number flows: Decoupling model. Phys Rev E 2007;75:036704.
[9] Prasianakis NI, Karlin IV. Lattice Boltzmann method for simulation of compressible flows on standard lattices. Phy Rev E 2008;78:016704.
[10] Chen Y, Ohashi H, Akiyama M. Thermal lattice Bhatnagar-Gross-Krook model without nonlinear deviations in macro-dynamic equations. Phys Rev E 1994;50:2776–83.
[11] Shan XW, Yuan XF, Chen HD. Kinetic theory representation of hydrodynamics: a way beyond the Navier-Stokes equation. J Fluid Mech 1994;550:413–41.
[12] Scagliarini A, Biferale L, Sbragaglia M, Sugiyama K, Toschi F. Lattice Boltzmann methods for thermal flows: continuum limit and applications to compressible rayleigh-taylor systems. Phys Fluids 2010;22(5):055101.
[13] Philippi PC, Hegele LA Jr, Santos LOD, Surmas R. From the continuous to the lattice Boltzmann equation: the discretization problem and thermal models. Phys Rev E 2006;73(5):056702.
[14] Siebert DN, Hegele LA, Philippi PC. Lattice Boltzmann equation linear stability analysis: thermal and athermal models. Phys Rev E 2008;77:026707.
[15] Nie X., Shan X, Chen H. Lattice Boltzmann/finite-difference hybrid simulation of transonic flow. AIAA Paper 2009; 139.
[16] Lew PT, Najafi-Yazdi A, Mongeau L. Unsteady numerical simulation of a round jet with impinging micro-jets for noise suppression. J Acoust Soc Am 2013;134(3):1982–9.
[17] Dubois F. Stable lattice Boltzmann schemes with a dual entropy approach for mono-dimensional nonlinear waves. Comput Math Appl 2013;65(2):142–59.
[18] Feng Y, Sagaut P, Tao W. A three dimensional lattice model for thermal compressible flow on standard lattices. J Comput Phys 2015;303:514–29.
[19] Feng Y, Tao WQ. A compressible thermal lattice Boltzmann model with factorization symmetry. Numer Heat Tr, Part B: Fund 2014;66(6):544–62.
[20] Frapolli N, Chikatamarla S, Karlin I. Multispeed entropic lattice Boltzmann model for thermal flows. Phys Rev E 2014;90(4):043306.
[21] Prasianakis NI, Karlin IV. Lattice Boltzmann method for thermal flow simulation on standard lattices. Phys Rev E 2007;76:016702.
[22] Li Q, Luo K, He Y, Tao W. Couplling lattice Boltzmann model for simulation of thermal flows on standard lattices. Phys Rev E 2012;85:016710.
[23] Hung L, Yang J. A coupled lattice Boltzmann model for thermal flows. IMA J Appl Math 2011;76:774–89.
[24] Karlin IV, Sichau D, Chikatamarla SS. Consistent two-population lattice Boltzmann model for thermal flows. Phys Rev E 2013;88:063310.
[25] Wolf-Gladrow DA. Lattice-gas cellular automata and lattice Boltzmann models: an Introduction. New York: Springer; 2000.
[26] Guo Z, Wang R, Xu K. Discrete unified gas kinetic scheme for all Knudsen number flows. II. Thermal compressible case. Phys Rev E 2015;91:033313.
[27] Guo Z, Xu K, Wang R. Discrete unified gas kinetic scheme for all Knudsen number flows: low-speed isothermal case. Phys Rev E 2013;88:033305.
[28] Wang P, Zhu L, Guo Z, Xu K. A comparative study of LBE and DUGKS methods for nearly incompressible flows. Commun Comput Phys 2015;17:657–81.
[29] Kim KH, Kim C, Rho OH. Methods for the accurate computations of hypersonic flows: I. ausmpw+scheme. J Comput Phys 2001;174(1):38–80.
[30] Liepmann H, Roshko A. Elements of gas-dynamics, Dover books on aeronautical engineering series. New York: Dover Publications; 1957.
[31] Lax PD, Liu XD. Solution of two-dimensional Riemann problems of gas dynamics by positive schemes. SIAM J Sci Comput 1998;19(2):319–40.